Controlling the Spatiotemporal Self-Organization of Stimuli-Responsive Nanocrystals Under Out-of-Equilibrium Conditions

Patrick Damacet,[a] Elissa O. Shehayeb,[a] and Katherine A. Mirica[a]*

a. Department of Chemistry, Burke Laboratory, Dartmouth College, Hanover, New Hampshire 03755, United States

ABSTRACT: Self-organization under out-of-equilibrium conditions is ubiquitous in natural systems for the generation of hierarchical solid-state patterns of complex structures with intricate properties. Efforts in applying this strategy to synthetic materials that mimic biological function has resulted in remarkable demonstrations of programmable self-healing and adaptive materials. However, the extension of these efforts to multifunctional stimuli-responsive solid-state materials across defined spatial distributions remains an unrealized technological opportunity. This paper describes the use of a nonequilibrium reaction–diffusion process to achieve the synthesis of a multifunctional stimuli-responsive electrically conductive metal–organic framework (cMOF) in a gelled medium with control over particle size and spatial periodicity on a macroscopic scale. Upon integration into chemiresistive devices, the resulting cMOF particles exhibit a size-dependent response towards hydrogen sulfide gas, as determined by their distinct surface-to-volume ratio, porosity, unique synthesis methodology, and unusual microcrystallite morphology compared to their counterparts obtained through bulk solution phase synthesis. Taken altogether, these achievements pave the way towards gaining access to functional nanomaterials with well-defined chemical composition, dimensions, and precisely tailored functions using far-from equilibrium approaches.

1. Introduction

Out-of-equilibrium self-organization of matter in precipitation reactions is pervasive in nature across multiple length scales.[1-4] This dynamic process plays an indispensable role in the mode of function of living organisms,[5] and is responsible for the formation of inorganic patterns of calcium carbonate crystals in mollusk shells and lime mortars,[6,7] the distribution of melanin pigment in zebra stripes,[4] as well as the intricate organization of microtubules,[8] stalactites,[9] and agates[10] in nature. This self-organization reflects the unique ability of these systems to assemble their molecular components into permanent patterns of hierarchical structures with multiscale functionalities that outperform their in-equilibrium counterparts.[11] The desire to harness chemical principles that govern out-of-equilibrium natural systems has inspired the development of novel approaches for producing hierarchically organized synthetic materials.[12-15] One of such synthetic approaches is the reaction-diffusion (RD) method, which involves the interplay between diffusion rates and reaction kinetics of unordered molecular components to generate well-defined spatial patterns of materials characterized by their ability to self-replicate and communicate continuously over space and time.[16] While this strategy has proven to be a powerful tool for the generation of smart materials in laboratory settings, including ionic skin,[13] cell signaling circuits,[17] and surface enhanced Raman scattering detection platforms,[18] extending this method to produce molecularly precise multifunctional materials with emergent programmable function in solid-state devices remains an unresolved challenge.[19]

Electrically conductive two-dimensional (2D) metal–organic frameworks represent an emerging class of porous crystalline materials with multifunctional characteristics that merge intrinsic conductivity, permanent porosity, and structural modularity with diverse function.[20] Benefitting from the merits of their extended in-plane conjugation and out-of-plane layered stacking, this class of materials has been widely integrated in (opto)electronic and energy devices for applications spanning spintronics,[21,22] rechargeable ion batteries and fuel cells,[23,24] electrocatalysis,[25,26] as well as simultaneous sensing, filtration, and detoxification of toxic gases.[27,28] Despite their broad potential utility, the current mode of preparation of this class of materials, encompassing primarily solution-based self-assembly processes,[29,30] has hindered strategic efforts into realizing control over their molecular design, and therefore, the understanding of their structure–property interconnections. As such, the development of novel approaches to access such framework materials with adaptive, dynamic, and sensing properties over macroscopic and molecular levels is highly needed.[31,32]

Herein, we report the first use of a non-equilibrium RD approach to achieve macroscopic periodic patterning of conductive metal–organic framework (cMOF) nanocrystals in a hydrogel medium via a periodic precipitation reaction. This method offers at least four unique attributes compared to the conventional methods currently used for synthesizing and patterning MOF materials on substrates.[33] First, it allows the generation of particle size libraries of a model 2D cMOF with distinct physicochemical properties such as surface areas and aspect ratios, in a one pot synthetic route. Conversely, conventional methods for producing MOFs with controlled properties often require multi-step synthetic procedures, utilization of additives, and distinct temperature conditions.[34-36] Second, this method produces a

high-resolution distribution of $Ni_3(HITP)_2$ (HITP = 2,3,6,7,10,11-hexaiminotriphenylene) nanostructures over macroscopic length scales, from which the various particle size libraries can be isolated. Their subsequent integration into functional sensing devices allows the investigation of structure–property interconnections by examining the preeminent conditions pivotal for maximizing the sensing capabilities of 2D cMOFs.[37, 38] Third, it provides fundamental insights into the self-assembly mechanism of $Ni_3(HITP)_2$ crystals from their molecular precursors into crystalline structures via spatiotemporal and structural analyses. Fourth, it is adaptable to predesigned macroscopic geometries and dimensions without the need for specialized instrumentation, making it a cost-effective approach.[39] We generate precipitation patterns of $Ni_3(HITP)$ via a Liesegang RD process by diffusing nickel ions into an agar gel column containing the organic ligand. We demonstrate that macroscopic pattern formation in the RD system is governed by a set of empirical scaling laws, which defines the periodicity, diffusive mechanism, and mass transfer characteristics of the overall RD system. Our results indicate that macroscopic pattern formation occurs during the nucleation of the MOF particles, which is a defining characteristic of a Liesegang prenucleation model.[40] The spatiotemporal resolution of the permanent periodic patterns of MOF nanocrystals within the gel matrix enables the isolation of particles of $Ni_3(HITP)_2$ with precisely controlled dimensions spanning from the nano- to the micro-scale. We demonstrate that this dimensional control influences the electrically transduced sensing function of this material towards hydrogen sulfide (H_2S), a reducing toxic gas, with an increase in the theoretical limit of detection (LoD) exceeding one-order of magnitude, going from 22 ± 4 ppb for the smallest particles to 384 ± 116 ppb for the largest ones. Taken together, our findings demonstrate the utility of hierarchical self-organization based on non-equilibrium processes for gaining access to functional nanomaterials with well-defined chemical composition, dimensions, and precisely tailored function.

2. Experimental design

Choice of MOF material

We selected $Ni_3(HITP)_2$ as a model system for patterning layered cMOFs in a hydrogel medium for three major reasons (**Figures 1a and S1**). First, the high intrinsic conductivity and ease of synthesis of $Ni_3(HITP)_2$ make this material broadly applicable in subfields of materials science in the context of chemical sensing,[41] electrocatalysis,[26] rechargeable batteries, supercapacitors, and electromagnetic wave absorption.[24, 42] Second, while the importance of controlling the crystal size and morphology of $Ni_3(HITP)_2$ has been shown to impact the functional performance of this material, methods for reliable synthetic control over its structural features remain extremely limited.[34] Third, the relatively high stability and solubility of its building blocks under ambient conditions allows for its processing in hydrogel media.[43]

Choice of the preparation method

Liesegang-type periodic precipitation reactions are typically carried out in porous hydrogel media by diffusing one of the reactants, generally the cation, into a gel matrix containing the complementary reactant.[44] The gel, as a supporting medium for pattern formation has at least two main roles. First, it reduces disruptive convective currents and hydrodynamic instabilities during the RD process, enabling the formation of robust Liesegang patterns (LPs).[40] Second, it attenuates the kinetics of the growing crystals along the tubular reactor, triggering nucleation and particle growth at specific sites. As a result, a gradient of immobilized MOF crystals with distinct sizes and physicochemical features can be generated in defined regions for detailed studies of structure–property interconnections.[45] We opted to use agar gel throughout this study due to its i) high porosity,[46] ii) chemical compatibility with 2,3,6,7,10,11-hexaaminotriphenylene hexahydrochloride (HATP·6HCl), and iii) transparent appearance, making a visual inspection of transport rates and pattern formation possible. We employed a 7:3 volume ratio of deionized (DI) water:*N*,*N*-dimethylformamide (DMF) throughout the study to ensure that the starting precursors are well dissolved and the reaction is proceeding homogeneously. While DI water is necessary to effectively dissolve agar gel and facilitate the diffusion of nickel ions into the gel, DMF as an organic polar aprotic solvent, enhances the solubility of the organic ligand, and thus ensures a homogeneous reaction environment. Additional information regarding the preparation procedures can be found in **Figures S2-S3** and **Section 2** of the SI.

3. Results and discussion

$Ni_3(HITP)_2$ LPs formation and characterization

Previous endeavors into the mechanism of formation of LPs indicated that a careful control over the chemical composition of the reaction media is required to trigger nucleation and subsequently particle growth over space and time.[47] Our preliminary optimization efforts suggested a procedure where diffusing 150 mM of nickel acetate ($Ni(OAc)_2$) into a 1% agar gel matrix containing a combination of 10 mM HATP·6HCl and 100 molar eq. of sodium acetate (NaOAc), with respect to the ligand, in a 7:3 volume ratio of DI water:DMF achieved the best pattern structure in terms of band separation and diffusion extent (**Figures S4-S8**). We began our investigations under this condition by examining the reaction dynamics and spatiotemporal arrangement of patterns observed in **Figure 1b-c** using a set of established mathematical models represented as empirical scaling laws, which included the i) spacing law, ii) time law, and iii) Matalon-Packter law (**Figure 2**).[40] Applying the Jabłczyński spacing law provided insight into the spatial periodicity and allowed for the calculation of the spacing coefficient (1+p) according to **Equation S1**. The linear correlation between the inter-band distances ($\Delta x_n = x_{n+1} - x_n$) revealed a regular patterning of the LPs, as evidenced by the calculated magnitude of 1+p of 1.078 (**Figures 2a and S9**).[48] Evaluation of the temporal dynamics of LP formation using the time law given by Morse and Pierce[49] according to **Equation S2** showed a linear relation between band position (x_n) and the square root of time ($\sqrt{t}$), as displayed in **Figures 2b and S10**. Given this law being analogous to the Einstein–Smoluchowski relation for a one-dimensional Brownian motion of particles in homogeneous space,[50] we calculated the effective diffusion coefficient (D_{front}) of the invading ions according to **Equation S3**, which yielded a D_{front} of 8.1 x 10^{-6} cm^2 s^{-1}, confirming the fast pattern dynamics and relative high concentration gradient of Ni^{2+} ions in the agar medium.[51] Overall, these results suggested that agar maintains a relatively high stability during the MOF self-organization

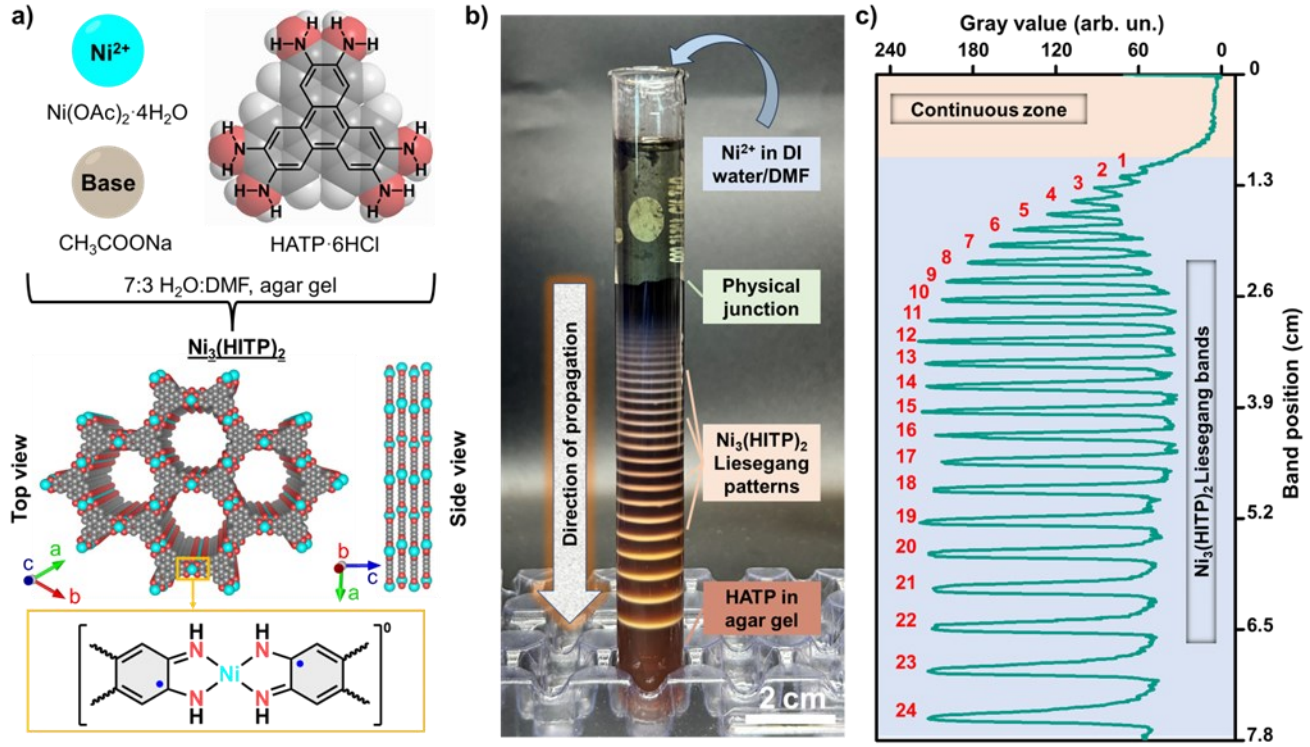

Figure 1. a) Space filling drawings of the simulated single crystal structure of $Ni_3(HITP)_2$ MOF with top and edge-site views along with its starting building blocks (HATP·6HCl ligand and Ni^{2+} ion), solvent mixture, and a close-up view of the diradical Ni-bisdiimine linkages. Color codes: Ni, ice blue; C, gray; N, red. H atoms are omitted for clarity. b) Spatio-temporal profile of Ni3(HITP)2 precipitation patterns in agar, generated via the RD approach by diffusing Ni^{2+} into an agar column containing HATP·6HCl and CH_3COONa in a 7:3 volume ratio of DI H_2O:DMF. c) Line profile analysis of the tubular reactor constructed following the conversion of the original image to an 8-bit grayscale image.

process, as evidenced by the formation of undisrupted, well-defined LPs across the entire reaction zone. The alignment of these patterns with empirical models indicated that the thermal stability and viscosity of the agar gel remain sufficiently unchanged throughout the reaction period.[52]

Examining the quantitative dependency of 1+p on the initial concentration of Ni^{2+} using **Equation S4** revealed an inverse correlation, which was consistent with the expectation from the Matalon–Packter law,[53] suggesting a decrease in the periodicity with increasing [Ni^{2+}] (**Figures 2c and S11-S12)**. Inspecting the spacing and time law plots for the reactors at different Ni^{2+} concentrations, shown in **Figures S13-S30**, revealed i) a linear correlation between D_{front} and [Ni^{2+}] and ii) a linear dependency of 1+p on the reciprocal of D_{front}, which were consistent with other Liesegang precipitation systems reported in the literature (**Figures S31-S32, and Table S1**).[53-55] Taken together, the strong agreement with the scaling laws accompanied by the lack of evident inner-band precipitates suggested that the processes of nucleation and MOF particle growth govern the band formation mechanism, and therefore, implied a pre-nucleation model describing the Liesegang precipitation reaction. Under this model, Ni^{2+} ions diffuse into the gel matrix and react with deprotonated HATP to form bands of $Ni_3(HITP)_2$ via nucleation and growth processes in the regions at which the product concentration of both, Ni^{2+} and HATP exceeds the nucleation threshold of the MOF.[40] As such, the positions of the precipitation bands and depleted regions are fixed at the nucleation and growth steps, with no solid precipitate forming in-between bands.[39] **Figure S33a** displays time-dependent snapshots of the reaction-front between 240 and 270 hours, capturing the formation of the 14th band in the reactor. While initially missing at the 240th hour mark, the band started to appear at the 250th hour mark as a light-colored, incomplete ring, before taking its final form after 270 hours, suggesting the completion of the precipitation reaction at that region. Line profile analysis of the 14th band revealed an increase in the grayscale value over time in proportion to the precipitate density (**Figure S33b**). This observation, coupled with the finding that the grayscale values and band positions of the preceding precipitations remained intact, confirmed our hypothesis of a pre-nucleation model governing the RD system (**Figure S34**).

To estimate the change in the concentration of Ni^{2+} over time following its diffusion into the gel matrix in the original RD system shown in **Figure 1b**, we carried out numerical simulations of ion diffusion on the basis of Fick's second law according to **Equation S5**.[56] To this end, we recorded the time course of the diffusion gradient by simulating the change in [Ni^{2+}] with time at 24 hour increments. Our results, depicted in **Figure S35**, suggested that Ni^{2+} could diffuse up to 3 cm into the gel matrix during the first 24 hours of reaction before depleting, as the diffusion profile progresses towards the edge of the reactor. Despite our experimental results suggesting the formation of the last band in the tubular reactor at a distance of 1.1 cm from the junction, following 24 hours of diffusion, our theoretical estimations implied the presence of a concentration gradient of Ni^{2+} in the agar medium past this band. Nonetheless, due to its low intensity, the coupling of this concentration gradient to the precipitation reaction was not possible, rendering band formation less likely to occur beyond this point.[47]

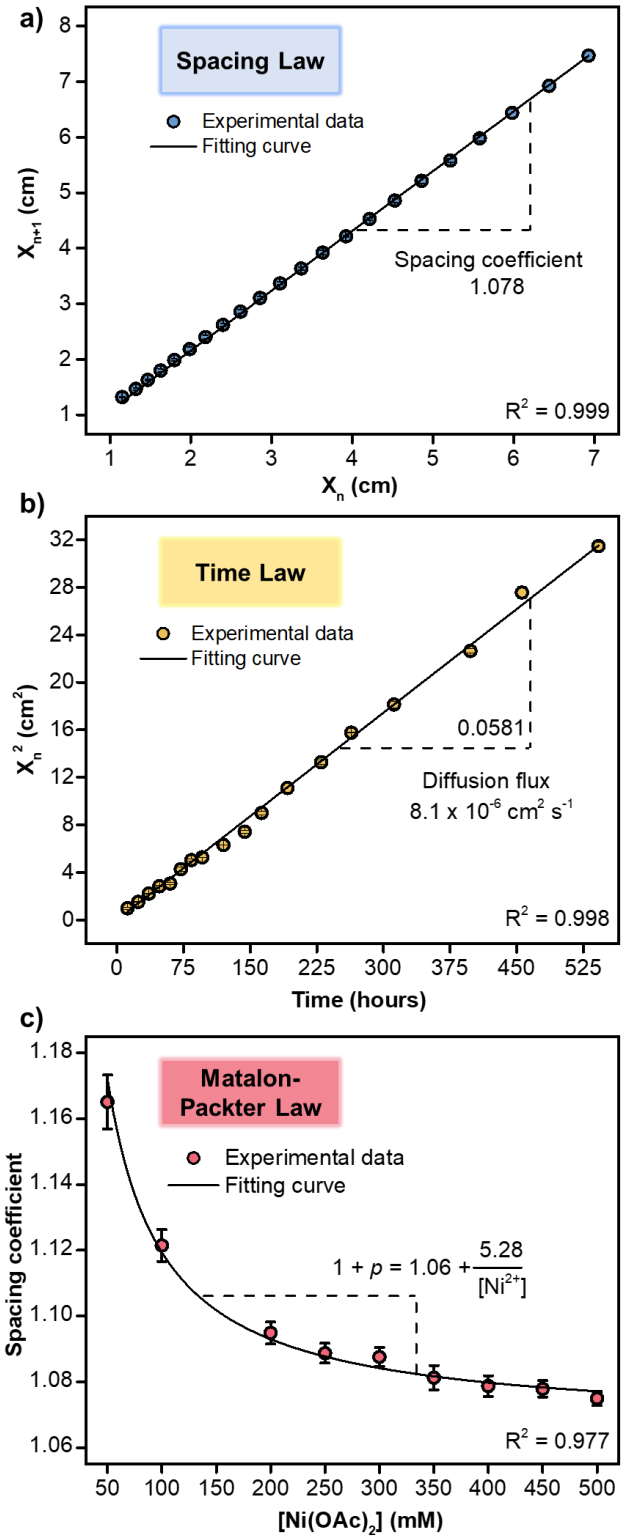

Figure 2. Verification of the empirical a) spacing law, b) time law, and c) Matalon-Packter law for the LPs formation in the RD system. Error bars represent the standard deviation of two measurements.

Morphological features and particle size distribution of $Ni_3(HITP)_2$ precipitates

With a clear picture of the optimal reaction conditions needed to produce Liesegang banding, we turned our attention towards characterizing the solid precipitates generated in the RD system. We isolated six precipitation zones from the tubular reactor, washed off the gel, and inspected the structural and morphological features of the resulting solid precipitates (Refer to **Figure 3a** and **Section S7** for more information). Powder x-ray diffraction (PXRD) measurements revealed the formation of highly crystalline $Ni_3(HITP)_2$ particles in all zones, as evidenced by the high relative intensity and well-matched peak positions compared to the patterns of bulk $Ni_3(HITP)_2$ prepared via a reported solvothermal method (**Figure 3b**).[57] Estimating the interplanar and interlayer distances of the crystals using Bragg's law revealed no significant changes in the geometric parameters of the molecular structure of the MOF crystals extracted from different zones (**Figure S36**). Scanning electron microscopy (SEM) images of the precipitates, displayed in **Figures 3d** and **S37-S38** indicated the formation of rice-shaped rods amassing nanosized irregular grains. The dimensions of these rods appeared to increase in both length and width moving away from the interface, as summarized in **Figure 3c**. While this size trend is found to be marginally significant, we attributed it to the non-linear change in the rates of nucleation and growth of the MOF particles along the spatial coordinate.[39, 40] At the interface where the concentration of Ni^{2+} ions is at its highest, Ni^{2+} and deprotonated HATP rapidly nucleate to form $Ni_3(HITP)_2$ colloidal seeds, characterized by the formation and partial stacking of oligomeric species,[58, 59] as evidenced by the length-to-width aspect ratio of 3.7 for the particles extracted from the interface. As the concentration of Ni^{2+} decreases moving away from the junction, nucleation is suppressed, rendering particle growth more favorable by the elongation of existing MOF seeds through π-stacking interactions along the *c-axis* of the crystals,[60] resulting in particles extracted from the 5th zone having a length-to-width aspect ratio of 6.8. However, the specific anisotropic features of this system complicate the simultaneous understanding of polymerization and crystallization processes governing the growth of $Ni_3(HITP)_2$ particles, as is the case for structurally similar 2D materials, like COF-5.[61, 62]

Macro- and micro-scopic analyses of $Ni_3(HITP)_2$ LPs under different chemical environments

We investigated the influence of solvent polarity on the morphology and periodicity of the $Ni_3(HITP)_2$ LPs by 1) increasing the volume ratio of DMF-to-DI water (φ_{DMF}) and 2) substituting DMF with dimethylacetamide (DMAC) and dimethyl sulfoxide (DMSO). Increasing φ_{DMF} from 0.3 to 0.6 resulted in i) an exponential increase in 1+p, ii) the appearance of less LPs throughout the gel medium, accompanied by a decrease in the extent of diffusion of nickel ions, and iii) formation of a MOF precipitate in the inter-band regions of the reactor (**Figures S39-S41**). These modifications, however, did not lead to any changes in the crystallinity or the global structure of the obtained $Ni_3(HITP)_2$ LPs, where regular-type LPs satisfying the spacing law plots were attained under all conditions (**Figures S42-S45**). To add, while substituting DMF with DMAC and DMSO did not result in any noticeable changes in the crystallinity of the MOF particles, inter-band precipitation regions were observed in the case of DMSO (**Figures S46-S53**). Previous studies have suggested that precipitation occurring in-between bands primarily results from the competitive formation of other

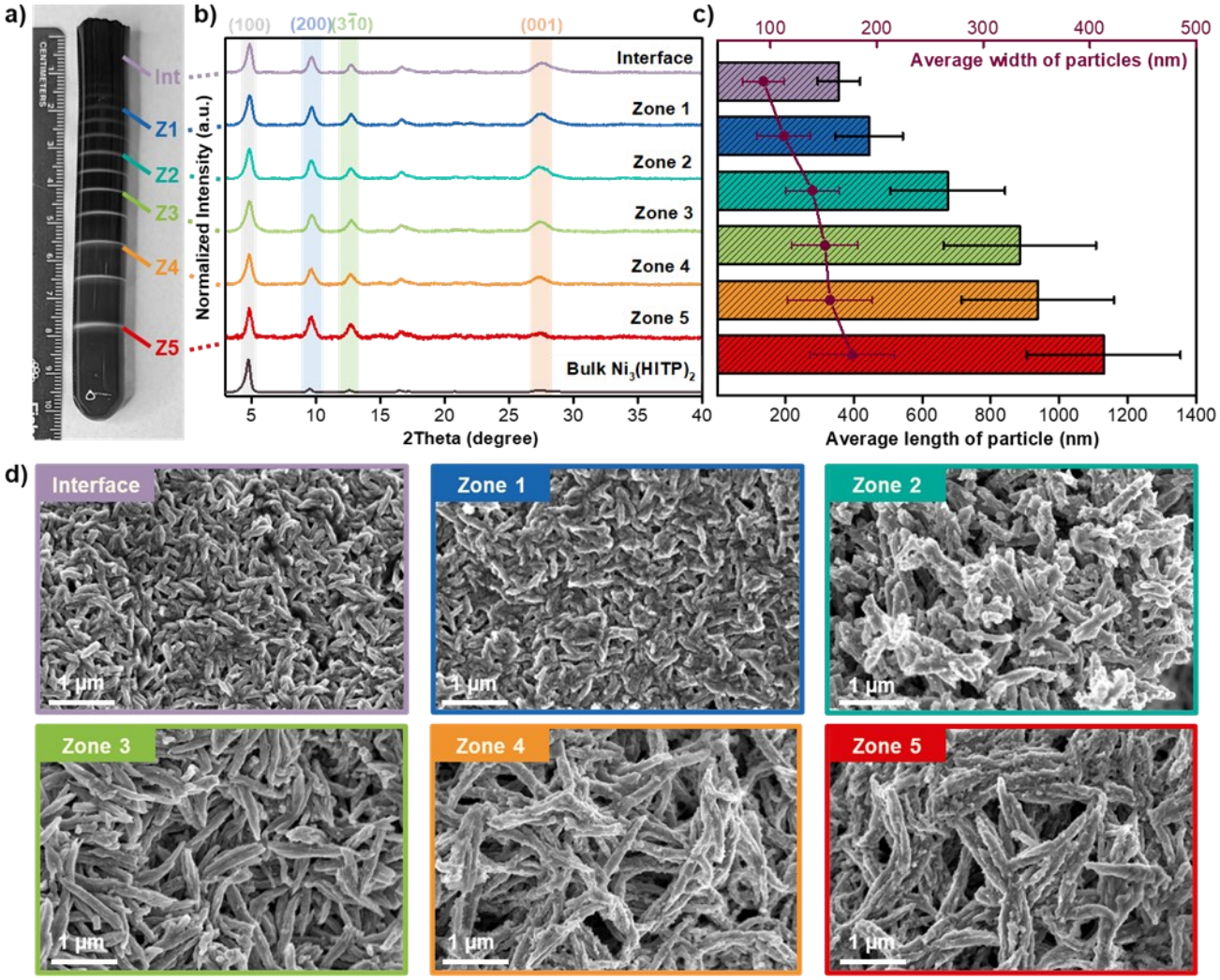

Figure 3. a) LPs of $Ni_3(HITP)_2$ MOF formed in an agar gel medium at room temperature. b) PXRD patterns of the $Ni_3(HITP)_2$ crystals isolated from the six bands. c) Particle size distribution of the MOF crystals determined via ImageJ, with the error bars indicating standard deviation from the mean based on 60 individual particles from each zone, and d) SEM images of the MOF particles extracted from the previously pointed out zones in part a.

intermediate species that can alter the existing periodic precipitation pattern.[63, 64] As such, we hypothesized that the temporary formation of Ni^{2+}-DMSO complexes, slowed down the diffusion of Ni^{2+} in the agar matrix containing deprotonated HATP, leading to the occurrence of random nucleation sites of $Ni_3(HITP)_2$ throughout the gel medium observed as inter-band precipitates.[65, 66] To add, while increasing the agar concentration from 0.5 to 2.0 % w/w had no remarkable effect on the overall extent of the precipitation zone, it resulted in a slight decrease in 1+p from 1.105 ± 0.003 to 1.063 ± 0.004, as depicted in **Figures S54-S58**.

To gain mechanistic insights into the role of NaOAc in the precipitation system, we carried out RD reactions, both in the absence of NaOAc, and in the presence of ammonium hydroxide as a base. Photographs of the reactors taken 10 days after the start of the RD reaction revealed the formation of a small continuous precipitation zone across the reactor, with no apparent LPs. PXRD measurements of the resulting precipitates identified an amorphous material in the absence of NaOAc, and nickel(II) hydroxide in the presence of ammonium hydroxide (**Figures S59-S60**). Additionally, we inverted the chemical composition of the inner and outer electrolytes by diffusing HATP·6HCl into 1% w/w agar matrices of Ni^{2+} ions dissolved in each of the mixtures of DI water:DMF, DI water:DMSO, and DI water:DMAC. Despite no precipitation bands emerging in all tubular reactors, as indicated by the spatiotemporal profiles shown in **Figures S61-S63**, we noted the formation of crystalline MOF particles in the case where NaOAc was employed in the same medium as HATP·6HCl. Overall, these results suggested the importance of adding the base to the same medium as HATP·6HCl, which facilitates the deprotonation of the HCl adducts and amine groups of the ligand prior to the latter's coordination to Ni^{2+}, and thus promotes the nucleation and subsequent growth of the MOF crystals.[67]

2D Liesegang rings of $Ni_3(HITP)_2$

The main disadvantage of the 1D LP system is the limited reaction surface area, which resulted in poor mixing of the starting reactants and subsequently a low conversion rate of 11 %, even when using a larger 1D reactor (**Figures S64-S69**). One way to address this limitation is to add an additional spatial dimension to ameliorate the transport of electrolytes to the reaction sites. To demonstrate this approach, we prepared a thin gel film containing HATP·6HCl and NaOAc inner electrolytes in a circular reactor of diameter = 10 cm and height = 1 cm, and allowed nickel ions, placed in

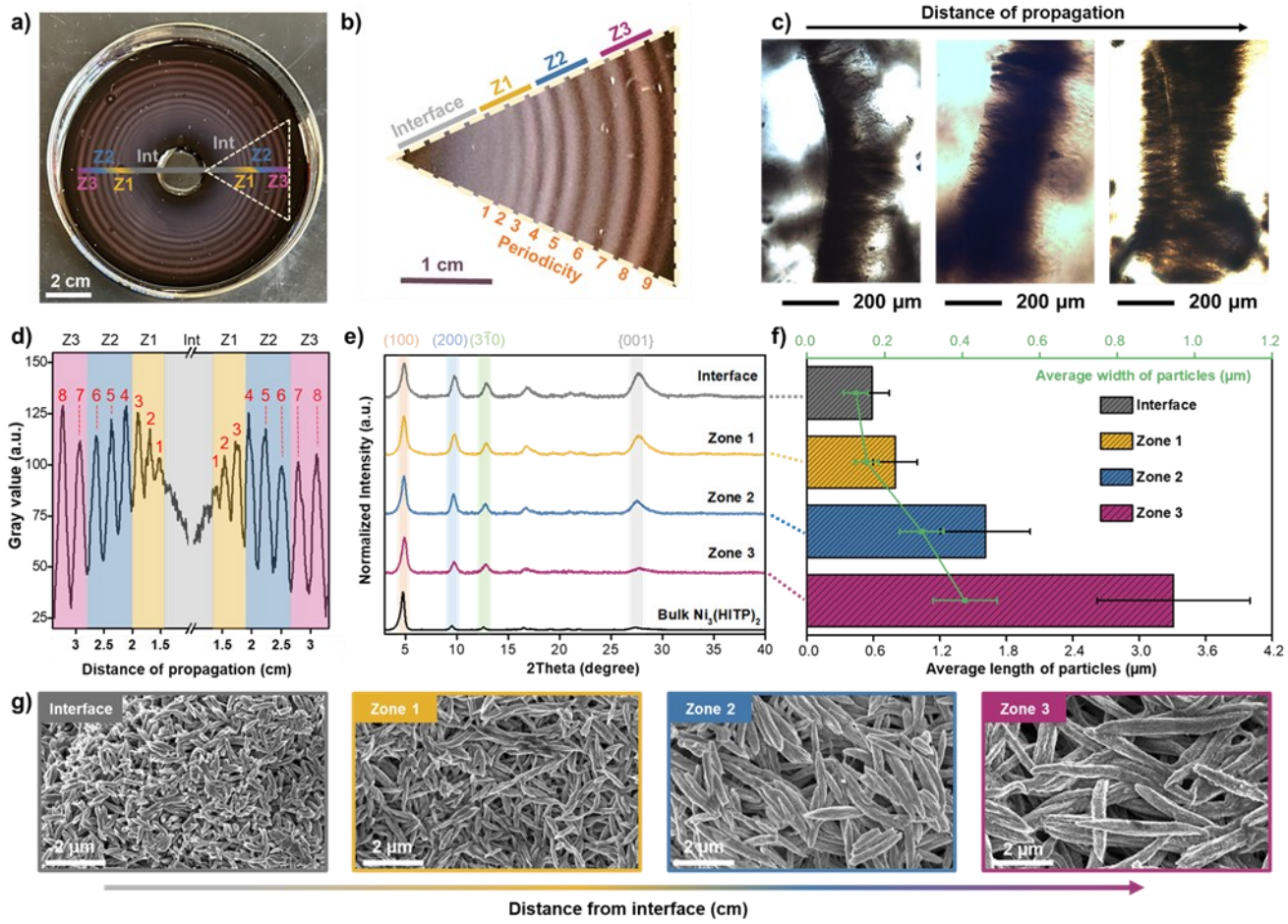

Figure 4. a) Representative spatial profile of $Ni_3(HITP)_2$ LRs generated in a 2D reactor. b) Line profile analysis of the LRs along with c) representative POM images of the rings formed at the liquid-gel interface. d) Photograph and e) PXRD patterns of the MOF particles isolated from each zone of the reactor. f) Particle size distribution of the MOF particles determined by ImageJ software with the error bars representing the standard deviation from the mean for 70 particles from each zone. g) SEM micrographs of the MOF particles isolated from each zone.

a groove at the center of the film, to diffuse onto the 2D plane over 7 days (**Figure S70**). We noted the formation of a continuous precipitation zone around the groove, followed by the emergence of discrete ring patterns farther away from the liquid-gel junction with an overall conversion rate exceeding 54 % (**Figures 4a and S71**). Line profile analysis of the resulting Liesegang rings (LRs) revealed an increase in the inter-band spacing as the diffusion profile progresses towards the edges of the circular reactor. Moreover, we found the spatiotemporal coordination of the LRs to obey both empirical scaling laws, which suggested a patterning mechanism similar to what we observed in the 1D system (**Figures 4b and S72-S74**). Polarized optical microscopy (POM) images of the LRs formed at the interface revealed an increase in the lateral dimensions of the rings towards the first precipitation zone, suggesting that the ring formation process began from a nucleation point at the liquid-gel junction from which periodic rings grew radially toward the edge of the reactor **(Figure 4c)**. These precipitation patterns contained rod-like crystals assembled in a circular arrangement around the circumference of the LRs, which in turn were aligned in the direction of the flow of nickel ions into the gel matrix (**Figure 4c**). While the *in-situ* observation of the MOF self-assembly process in the reactor was not the focus of this study, given the sensitivity of the hydrogel to moisture, POM images of the LRs provided evidence of the anisotropic alignment of the crystals in the gel matrix (**Figure 4c**).

To inspect the characteristic features of the obtained microstructures in the 2D reactor, we isolated four zones, each encompassing 2-3 precipitation rings from the gel film (**Figure 4d**). Similar to the 1D system, we noted the formation of highly crystalline $Ni_3(HITP)_2$ particles with prominent (100) and (200) crystallographic planes observed in PXRD and emergent rice-shaped nanorod morphology visualized by SEM (**Figure 4e-g**). Notably, the isolated MOF crystals were found to be significantly larger than those generated in the 1D reactor, with particles extracted 4 cm away from the junction having lengths spanning from 1.1 ± 0.2 µm in the 1D reactor, to 3.3 ± 0.6 µm in the 2D reactor (**Figures S75-S77**). We ascribed this result to the increased spatial dimensionality in the circular reactor, which led to a relatively rapid decrease of the supersaturation gradient of $[Ni^{2+}]$, shortening the nucleation process, and thereby promoting the growth of the MOF particles (**Figure S78**). Brunauer-Emmett-Teller (BET) surface area measurements, shown in **Figure S79** revealed a dramatic decrease in the surface area of the MOF particles going away from the interface, which was consistent with the literature, given the inverse relation between the size of MOF particles and their surface area/volume ratio.[68, 69] Additionally, X-ray photoelectron spectroscopy (XPS), thermogravimetric

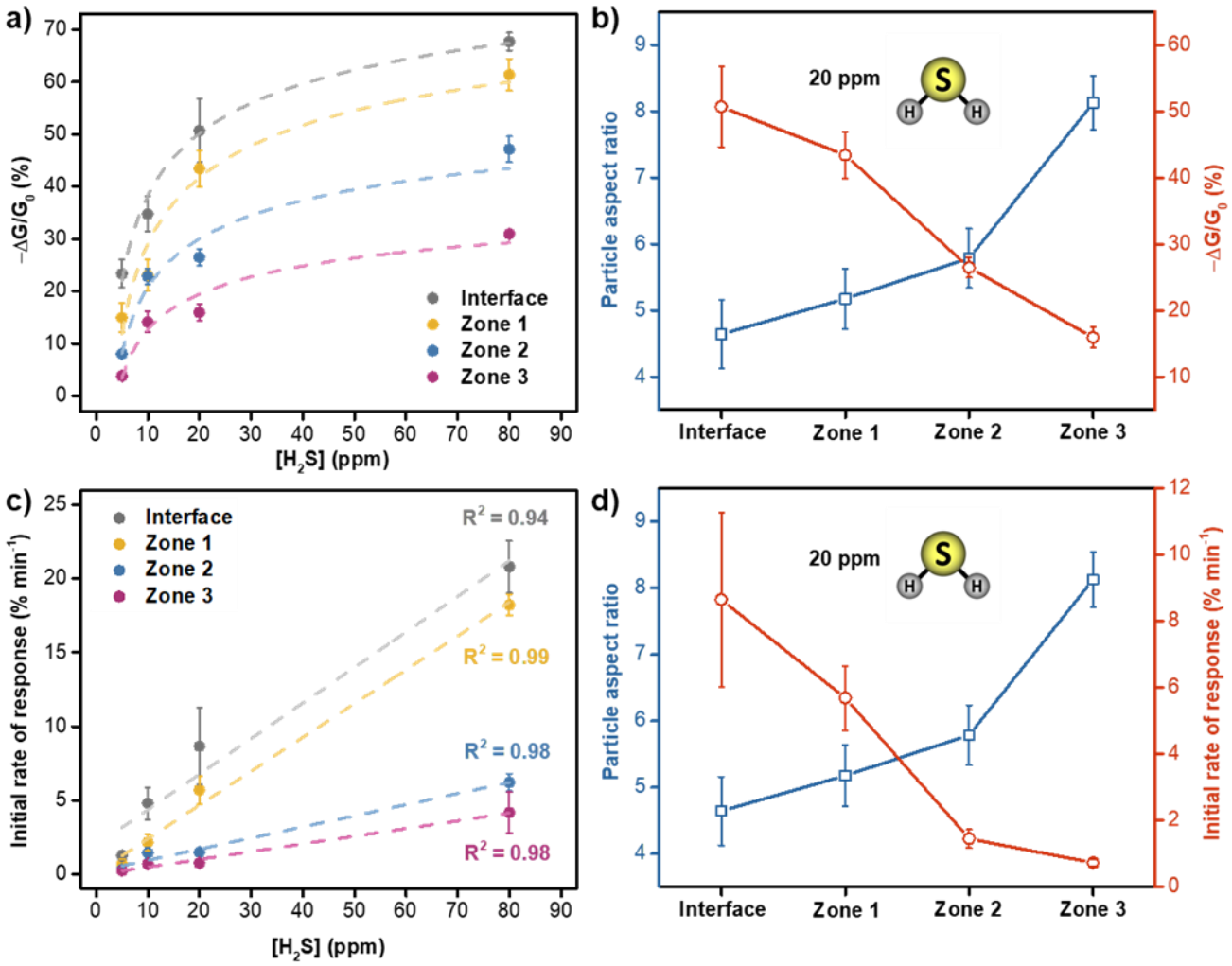

Figure 5. a) Normalized chemiresistive responses of devices integrated with $Ni_3(HITP)_2$ particles isolated from four zones of the 2D reactor to H_2S at different concentrations, under an applied voltage of 0.1 V. b) Correlation between length-to-width aspect ratio of $Ni_3(HITP)_2$ particles and H_2S sensing response at 20 ppm. c) Correlation between the initial rate of response ($-\Delta G/G_0$)/Δt(min)) and H_2S concentrations during the first 1 min of analyte exposure. d) Correlation between length-to-width aspect ratio of $Ni_3(HITP)_2$ particles and H_2S sensing response at 20 ppm during the first 1 min of analyte exposure.

analysis (TGA), and 4-point probe conductivity measurements implied similar chemical composition, electrical properties, and thermal stabilities for the MOF particles (**Figures S80-S83, Tables S2-S4**).[57]

Chemiresistive detection of H_2S using size-controlled $Ni_3(HITP)_2$ nanocrystals

Encouraged by the ability to generate particle size libraries of $Ni_3(HITP)_2$ with similar electrical properties, we investigated the chemiresistive performance of these crystals as a function of particle size. We selected H_2S as a model analyte due to its significance as both, a biological signaling molecule and an environmental pollutant, particularly in contaminated hot springs, gas wells, and wastewater treatment plants.[70] At mid-to-high-ppm levels, H_2S exposure gives rise to a wide array of health effects, ranging from headache and dizziness, to eye and respiratory tract irritation, making it an important target for sensing applications.[71] While $Ni_3(HITP)_2$ has been previously used to achieve detection of H_2S,[28, 41] the understanding of the sensing mechanism and the role of crystal size in determining the sensing properties of this material has remained largely unclear. We prepared chemiresistive devices by dropcasting 20 µL of aqueous $Ni_3(HITP)_2$ suspensions (1 mg mL^{-1}) onto interdigitated 5 µm gap gold electrodes, which generated devices with resistances in the range of ~0.1-0.5 KΩ (**Section S11**). After loading the devices into our custom-built gas sensing cell and conditioning them under constant electrical bias and nitrogen flow, we monitored the current change upon exposure to the gas analyte at a driving voltage of 0.1 V through direct-current amperometric (I–t) measurements at room temperature (**Figures S84-S86**).

As illustrated in **Figure 5a-b**, $Ni_3(HITP)_2$ devices exhibited a systematic size-dependent response towards H_2S with the smallest particles, extracted from the interface, displaying the highest sensing response ($-\Delta G/G_0$) upon exposure to a range of H_2S concentrations (5–80 ppm) for 30 mins. Given 1) the nonalignment of the conductivity of this material with its particle size (**Table S4**), and 2) the affirmation from previous reports that the impact of surface area and morphology of $Ni_3(HITP)_2$ on its electrochemical behavior is more prominent than the effect of its bulk electrical conductivity,[34, 72] we attributed the inverse size-

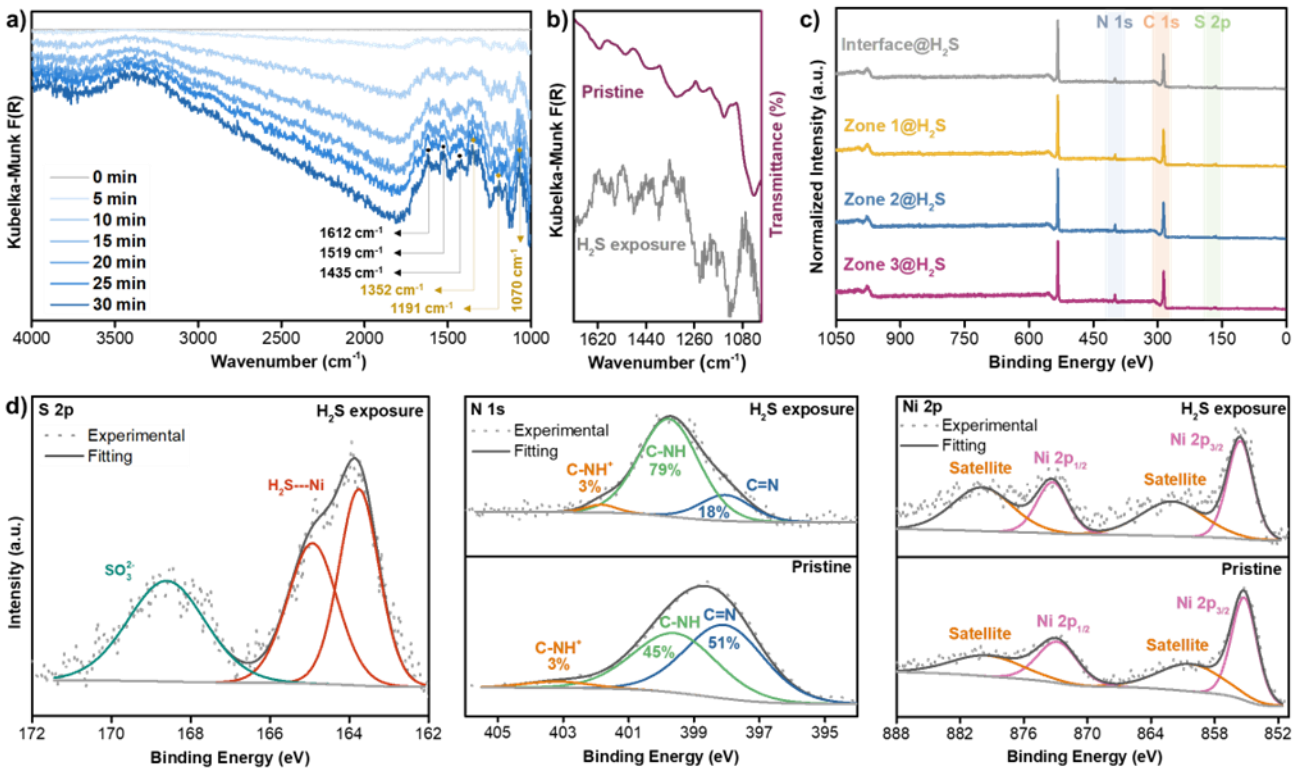

Figure 6. Spectroscopic probing of the electronic response of $Ni_3(HITP)_2$-Interface towards H_2S analyte. a) Kubelka–Munk transformed DRIFTS of MOF particles after exposure to 0.1% H_2S in N_2 for 30 mins. b) Comparison of the difference spectrum of the MOF upon 30 min exposure to H_2S to the transmittance of the pristine MOF. c) XPS survey of H_2S-exposed $Ni_3(HITP)_2$ particles extracted from the 2D LR reactor, and d) High-resolution XPS spectra of sulfur (S 2p), nitrogen (N 1s), and nickel (Ni 2p) elements for the $Ni_3(HITP)_2$-Interface particles upon exposure to 1% H_2S in N_2 for 2 hrs.

response interconnection to the relatively high surface area of the smaller particles extracted from the junction compared to the large particles isolated away from the interface, which translates into a higher density of favorable gas adsorption sites, and thus stronger and faster intermolecular interactions between the analyte and the framework (**Figures S87-S92**).[73-75] We corroborated this observation by analyzing the initial rates of response of $Ni_3(HITP)_2$ devices following a 1-minute exposure to 20 ppm of H_2S. As displayed in **Figures 5c-d and S93-S97**, we noted a 12-fold increase in the initial response rate of the particles extracted from the interface (8.7 ± 2.6 % min^{-1}), which exhibited the smallest length-to-width aspect ratio (4.6 ± 0.5), and highest surface area (354 ± 7 m^2 g^{-1}) compared to the particles extracted from Zone 3 (0.7 ± 0.1 % min^{-1}), which had the largest length-to-width ratio (8.2 ± 0.4) as well as lowest surface area (51 ± 1 m^2 g^{-1}). These results were further confirmed by energy dispersive X-ray (EDX) measurements of the MOF-deposited electrodes following H_2S exposure, which revealed a higher sulfur uptake (3.2 ± 0.49 %) for the interface particles compared to Zone 3 particles (0.45 % ± 0.11 %), suggesting a high density of favorable host sites between H_2S and the smallest particles (**Figures S98-S105**).

We assessed the mode of interactions between H_2S and the best performing MOF, that is $Ni_3(HITP)_2$ particles extracted from the interface via a suite of spectroscopic techniques. *In-situ* diffuse reflectance infrared Fourier transform spectroscopy (DRIFTS) spectra revealed the significant electronic and bond strengthening effect of H_2S on $Ni_3(HITP)_2$ upon their interaction. First, we noted a major shift in the baseline between 4000 and 2000 cm^{-1}, which we attributed to electronic absorption, confirming that strong electronic variations are occurring in the material in the presence of H_2S (**Figure 6a**).[76] Second, compared to the ATR-IR spectrum of the pristine MOF shown in **Figure 6b**, several peaks displayed a shift in intensity to higher wavenumbers, particularly those at 1036, 1149, and 1325 cm^{-1} to 1070, 1191, and 1352 cm^{-1}, respectively, attributed to the strengthening of the C-N stretching vibrations,[77] consistent with a previous report involving partial density of states (PDOS) findings of $Ni_3(HITP)_2$ upon exposure to H_2S.[78] Third, absorption bands relating to pristine MOF peaks, namely 1435 and 1519 cm^{-1} for C-C stretching vibrations and 1612 cm^{-1} for C=C stretching vibrations, appeared during gas exposure, meaning that their intensities sharpened in the presence of H_2S.[77] These results suggested the reducing effect H_2S is posing on the HATP ligand.[79] To add, *ex-situ* XPS analysis suggested the formation of sulfite and nickel sulfide species following H_2S exposure, as indicated by the emergence of new emission lines at binding energies of 163.7, 165.0 and 168.6 eV (**Figure 6d**). This observation suggested that both, the Ni nodes and HATP ligand play a role in the sensing mechanism as sulfite species are likely getting reduced to sulfide due to the oxidation of HITP.[41] We corroborated this hypothesis by estimating the peak area ratio of Ni-N-C to Ni-N=C moieties of the MOF following gas sensing, which revealed a 5-fold increase, signifying a change in the oxidation state of the ligand (**Figure 6d**). Overall, as HITP is being reduced upon exposure to H_2S, the optimal π-d orbital overlap in $Ni_3(HITP)_2$ is being disrupted, increasing the resistance of the material, observed as a decrease in current in the sensing response (**Figure S106**).

When normalized, it is plotted as an increase in negative normalized conductance.

Notably, the devices generated via the RD approach and extracted from the interface displayed a remarkably lower theoretical LoD (22 ± 4 ppb, refer to **Section 11.9** of the SI) and superior sensing performance, measured as 51 ± 6 % change in conductance upon exposure to 20 ppm of analyte, suggesting a strong sensitivity to H_2S that exceeds well-established room-temperature sensing materials.[80] In contrast, $Ni_3(HITP)_2$ devices prepared from the conventional solvothermal method reported in the literature, exhibited a considerably higher LoD (738 ± 23 ppb) and a lower response of 13 ± 3% change in conductance under the same conditions, as depicted in **Figures S107-S112**. We attributed this variation to the decrease in the level of coverage of the electrode interdigitations with the deposited MOF particles extracted from the interface to zone 3 and $Ni_3(HITP)_2$ synthesized solvothermally, as visualized previously in their SEM images. Remarkably, $Ni_3(HITP)_2$ did not undergo any significant structural changes even when exposed to 10,000 ppm H_2S for two hours, as opposed to other isostructural 2D cMOFs[27] (**Figures S113-S115**). These results asserted the valuable role of the RD approach in generating functionality-enhancing hierarchies of $Ni_3(HITP)_2$ microstructures with improved sensing characteristics compared to the reported bulk solution phase appraoches.[57] Finally, exposing all devices to 7 dosing/recovery sensing cycles at 80 ppm demonstrated the strong dosimetric character of the interaction of $Ni_3(HITP)_2$ with H_2S, where full saturation and limited recovery following analyte exposure were observed (**Figure S116**).

4. Conclusion

We presented an out-of-equilibrium strategy for the self-assembly and patterning of $Ni_3(HITP)_2$ MOF in a gelled medium. Our approach provided three innovative advantages in the context of MOF patterning over their traditional liquid-phase counterparts. First, the Liesegang precipitation reaction offered a way to gain a straightforward access to structural multi-level complexity in $Ni_3(HITP)_2$ through dynamic pathways coupled with non-linear kinetics. As such, it enabled control over the processes of nucleation and crystal growth, thus generating precisely controlled periodic patterns of $Ni_3(HITP)_2$ crystals over a macroscopic domain. Second, it allowed for the generation and isolation of spatially separated MOF crystals with distinct sizes and structural properties, ranging across one order of magnitude in length and width via a one pot synthetic route. Third, the access to $Ni_3(HITP)_2$ particles with controlled sizes enabled fundamental insight into the role that crystal length-width ratio and surface area plays in determining electrically transduced sensing responses of this material towards a reducing gas. Although our approach focused on a model system of layered conductive materials, extending it to other multifunctional materials and structures[81-83] should be feasible by considering the initial concentrations of precursors, gel type and viscosity, and solvent(s) characteristics. In our work, we found that ensuring solubility of the initial precursors is critical to systematic investigation of MOF formation via an RD methodology.

Overall, this study provides a novel design strategy towards the development of functionality-enhancing hierarchies of layered cMOFs under far-from-thermodynamic equilibrium conditions. The findings achieved herein align well with results from existing literature regarding the impact of particle size on their chemiresistive sensing performance.[74, 84] Employing small particles with high surface areas extracted from the interface minimized mass transfer resistance, thus ensuring unhindered, discrete adsorption and diffusion pathways for H_2S analyte into the active sensing sites of the MOFs. As such, hierarchical structuring was found to mitigate mass transfer limitations, enhancing both, the overall sensing performance of $Ni_3(HITP)_2$ and potential utility in other applications such as energy storage, drug delivery, and water remediation. Future studies that undertake strategic optimization of reaction conditions to make the RD approach amendable to other ligands and metal nodes has the potential to turn the periodic precipitation approach into a platform technology for producing highly tailored and modular multifunctional materials with precise control over their structure and function.

ASSOCIATED CONTENT

Supporting Information

The supporting information is available free of charge at http://pubs.acs.org.

Experimental methods, Liesegang scaling laws, morphological features of the MOF nanocrystals, effect of physicochemical parameters on the morphology and periodicity of LPs, H_2S sensing studies (PDF).

AUTHOR INFORMATION

Corresponding Author

Katherine A. Mirica - *Dartmouth College, Hanover, New Hampshire 03755, United States; orcid.org/0000-0002-8039-1405*; Email: Katherine.a.mirica@dartmouth.edu

Authors

Patrick Damacet - *Dartmouth College, Hanover, New Hampshire 03755, United States*; orcid.org/0000-0002-8039-1405

Elissa O. Shehayeb - *Dartmouth College, Hanover, New Hampshire 03755, United States*; orcid.org/0009-0006-6810-617X

Notes

The authors declare no competing financial interest.

ACKNOWLEDGMENTS

The authors gratefully acknowledge financial support from the Dartmouth Guarini School PhD Innovation Program, National Science Foundation CAREER award (#1945218), and National Science Foundation Research Traineeship award (#2125733). P.D. thanks Georganna Benedetto for the fruitful discussions regarding the sensing experiments.

5. References

1. Kondo, S.; Miura, T., Reaction-Diffusion Model as a Framework for Understanding Biological Pattern Formation. *Science* **2010,** *329* (5999), 1616-1620.
2. Epstein, I. R.; Xu, B., Reaction–diffusion processes at the nano- and microscales. *Nat. Nanotechnol* **2016,** *11* (4), 312-319.

3. Grzybowski, B. A.; Huck, W. T. S., The nanotechnology of life-inspired systems. *Nat. Nanotechnol* **2016,** *11* (7), 585-592.
4. Cass, J. F.; Bloomfield-Gadêlha, H., The reaction-diffusion basis of animated patterns in eukaryotic flagella. *Nat. Commun.* **2023,** *14* (1), 5638.
5. Adamski, P.; Eleveld, M.; Sood, A.; Kun, Á.; Szilágyi, A.; Czárán, T.; Szathmáry, E.; Otto, S., From self-replication to replicator systems en route to de novo life. *Nat. Rev. Chem* **2020,** *4* (8), 386-403.
6. Falini, G.; Albeck, S.; Weiner, S.; Addadi, L., Control of Aragonite or Calcite Polymorphism by Mollusk Shell Macromolecules. *Science* **1996,** *271* (5245), 67-69.
7. Rodriguez-Navarro, C.; Cazalla, O.; Elert, K.; Sebastian, E., Liesegang Pattern Development in Carbonating Traditional Lime Mortars. *Proc. Math. Phys. Eng. Sci* **2002,** *458* (2025), 2261-2273.
8. Hess, H.; Ross, J. L., Non-equilibrium assembly of microtubules: from molecules to autonomous chemical robots. *Chem. Soc. Rev.* **2017,** *46* (18), 5570-5587.
9. Short, M. B.; Baygents, J. C.; Beck, J. W.; Stone, D. A.; Toomey III, R. S.; Goldstein, R. E., Stalactite growth as a free-boundary problem: a geometric law and its platonic ideal. *Phys. Rev. Lett.* **2005,** *94* (1), 018501.
10. Heaney, P. J.; Davis, A. M., Observation and origin of self-organized textures in agates. *Science* **1995,** *269* (5230), 1562-1565.
11. Osat, S.; Golestanian, R., Non-reciprocal multifarious self-organization. *Nat. Nanotechnol* **2023,** *18* (1), 79-85.
12. Leathers, A.; Walczak, M.; Brady, R. A.; Al Samad, A.; Kotar, J.; Booth, M. J.; Cicuta, P.; Di Michele, L., Reaction–Diffusion Patterning of DNA-Based Artificial Cells. *J. Am. Chem. Soc.* **2022,** *144* (38), 17468-17476.
13. Qiao, H.; Sun, S.; Wu, P., Non-equilibrium-Growing Aesthetic Ionic Skin for Fingertip-Like Strain-Undisturbed Tactile Sensation and Texture Recognition. *Adv. Mater.* **2023,** *35* (21), 2300593.
14. Kubota, R.; Hamachi, I., Cell-Like Synthetic Supramolecular Soft Materials Realized in Multicomponent, Non-/Out-of-Equilibrium Dynamic Systems. *Adv. Sci* **2024,** *11* (8), 2306830.
15. Suslick, B. A.; Hemmer, J.; Groce, B. R.; Stawiasz, K. J.; Geubelle, P. H.; Malucelli, G.; Mariani, A.; Moore, J. S.; Pojman, J. A.; Sottos, N. R., Frontal Polymerizations: From Chemical Perspectives to Macroscopic Properties and Applications. *Chem. Rev.* **2023,** *123* (6), 3237-3298.
16. Boekhoven, J.; Hendriksen, W. E.; Koper, G. J.; Eelkema, R.; van Esch, J. H., Transient assembly of active materials fueled by a chemical reaction. *Science* **2015,** *349* (6252), 1075-1079.
17. Rajasekaran, R.; Chang, C.-C.; Weix, E. W. Z.; Galateo, T. M.; Coyle, S. M., A programmable reaction-diffusion system for spatiotemporal cell signaling circuit design. *Cell* **2024,** *187* (2), 345-359.e16.
18. Nenashkina, A.; Koltsov, S.; Orlova, O. Y.; Nikitina, A. A.; Kirilenko, D. A.; Andreeva, D. V.; Blanco-Formoso, M.; Pazos-Perez, N.; Alvarez-Puebla, R.; Skorb, E. V., Silver melamine thin film as a flexible platform for SERS analysis. *Nanoscale* **2021,** *13* (15), 7375-7380.
19. Knoll, P.; Ouyang, B.; Steinbock, O., Patterns Lead the Way to Far-from-Equilibrium Materials. *ACS Phys. Chem. Au* **2024,** *4* (1), 19-30.
20. Ko, M.; Mendecki, L.; Mirica, K. A., Conductive two-dimensional metal–organic frameworks as multifunctional materials. *Chem. Commun.* **2018,** *54* (57), 7873-7891.
21. Yan, X.; Su, X.; Chen, J.; Jin, C.; Chen, L., Two-Dimensional Metal-Organic Frameworks Towards Spintronics. *Angew. Chem. Int. Ed.* **2023,** *62* (41), e202305408.
22. Song, X.; Jin, C.; Chen, H.; Ding, S.; Liu, Z.; Li, Y.; Yan, X.; Mi, W.; Chen, L.; Hu, W., Two-Dimensional Conductive Metal–Organic Framework Reinforced Spinterface in Organic Spin Valves. *CCS Chem.* **2024,** *6* (1), 208-217.
23. Yang, M.; Zeng, X.; Xie, M.; Wang, Y.; Xiao, J.-M.; Chen, R.-H.; Yi, Z.-J.; Huang, Y.-F.; Bin, D.-S.; Li, D., Conductive Metal–Organic Framework with Superior Redox Activity as a Stable High-Capacity Anode for High-Temperature K-Ion Batteries. *J. Am. Chem. Soc.* **2024,** *146* (10), 6753-6762.
24. Cai, D.; Lu, M.; Li, L.; Cao, J.; Chen, D.; Tu, H.; Li, J.; Han, W., A Highly Conductive MOF of Graphene Analogue Ni3(HITP)2 as a Sulfur Host for High-Performance Lithium–Sulfur Batteries. *Small* **2019,** *15* (44), 1902605.
25. Meng, Z.; Luo, J.; Li, W.; Mirica, K. A., Hierarchical Tuning of the Performance of Electrochemical Carbon Dioxide Reduction Using Conductive Two-Dimensional Metallophthalocyanine Based Metal–Organic Frameworks. *J. Am. Chem. Soc.* **2020,** *142* (52), 21656-21669.
26. Mariano, R. G.; Wahab, O. J.; Rabinowitz, J. A.; Oppenheim, J.; Chen, T.; Unwin, P. R.; Dincă, M., Thousand-fold increase in O2 electroreduction rates with conductive MOFs. *ACS Cent. Sci.* **2022,** *8* (7), 975-982.
27. Eagleton, A. M.; Ko, M.; Stolz, R. M.; Vereshchuk, N.; Meng, Z.; Mendecki, L.; Levenson, A. M.; Huang, C.; MacVeagh, K. C.; Mahdavi-Shakib, A.; Mahle, J. J.; Peterson, G. W.; Frederick, B. G.; Mirica, K. A., Fabrication of Multifunctional Electronic Textiles Using Oxidative Restructuring of Copper into a Cu-Based Metal–Organic Framework. *J. Am. Chem. Soc.* **2022,** *144* (51), 23297-23312.
28. Smith, M. K.; Mirica, K. A., Self-Organized Frameworks on Textiles (SOFT): Conductive Fabrics for Simultaneous Sensing, Capture, and Filtration of Gases. *J. Am. Chem. Soc.* **2017,** *139* (46), 16759-16767.
29. Dou, J.-H.; Arguilla, M. Q.; Luo, Y.; Li, J.; Zhang, W.; Sun, L.; Mancuso, J. L.; Yang, L.; Chen, T.; Parent, L. R.; Skorupskii, G.; Libretto, N. J.; Sun, C.; Yang, M. C.; Dip, P. V.; Brignole, E. J.; Miller, J. T.; Kong, J.; Hendon, C. H.; Sun, J.; Dincă, M., Atomically precise single-crystal structures of electrically conducting 2D metal–organic frameworks. *Nat. Mater.* **2021,** *20* (2), 222-228.
30. Skorupskii, G.; Trump, B. A.; Kasel, T. W.; Brown, C. M.; Hendon, C. H.; Dincă, M., Efficient and tunable one-dimensional charge transport in layered lanthanide metal–organic frameworks. *Nat. Chem* **2020,** *12* (2), 131-136.
31. Matsuda, T.; Kawakami, R.; Namba, R.; Nakajima, T.; Gong, J. P., Mechanoresponsive self-growing hydrogels inspired by muscle training. *Science* **2019,** *363* (6426), 504-508.
32. England, J. L., Dissipative adaptation in driven self-assembly. *Nat. Nanotechnol* **2015,** *10* (11), 919-923.
33. Falcaro, P.; Buso, D.; Hill, A. J.; Doherty, C. M., Patterning Techniques for Metal Organic Frameworks. *Adv. Mater.* **2012,** *24* (24), 3153-3168.
34. Borysiewicz, M. A.; Dou, J.-H.; Stassen, I.; Dincă, M., Why conductivity is not always king – physical properties governing the capacitance of 2D metal–organic framework-based EDLC supercapacitor electrodes: a Ni3(HITP)2 case study. *Faraday Discuss.* **2021,** *231* (0), 298-304.
35. Snook, K. M.; Zasada, L. B.; Chehada, D.; Xiao, D. J., Oxidative control over the morphology of Cu3(HHTP)2, a 2D conductive metal–organic framework. *Chem. Sci.* **2022,** *13* (35), 10472-10478.
36. Huang, X.; Yao, H.; Cui, Y.; Hao, W.; Zhu, J.; Xu, W.; Zhu, D., Conductive Copper Benzenehexathiol Coordination Polymer as a Hydrogen Evolution Catalyst. *ACS Appl. Mater. Interfaces.* **2017,** *9* (46), 40752-40759.
37. Jo, Y.-M.; Jo, Y. K.; Lee, J.-H.; Jang, H. W.; Hwang, I.-S.; Yoo, D. J., MOF-Based Chemiresistive Gas Sensors: Toward New Functionalities. *Adv. Mater.* **2023,** *35* (43), 2206842.

38. Huang, C.; Sun, W.; Jin, Y.; Guo, Q.; Mücke, D.; Chu, X.; Liao, Z.; Chandrasekhar, N.; Huang, X.; Lu, Y.; Chen, G.; Wang, M.; Liu, J.; Zhang, G.; Yu, M.; Qi, H.; Kaiser, U.; Xu, G.; Feng, X.; Dong, R., A General Synthesis of Nanostructured Conductive Metal–Organic Frameworks from Insulating MOF Precursors for Supercapacitors and Chemiresistive Sensors. *Angew. Chem. Int. Ed.* **2024,** *63* (3), e202313591.
39. Nakouzi, E.; Steinbock, O., Self-organization in precipitation reactions far from the equilibrium. *Sci. Adv.* **2016,** *2* (8), e1601144.
40. Nabika, H.; Itatani, M.; Lagzi, I., Pattern Formation in Precipitation Reactions: The Liesegang Phenomenon. *Langmuir* **2020,** *36* (2), 481-497.
41. Lee, T.; Kim, J.-O.; Park, C.; Kim, H.; Kim, M.; Park, H.; Kim, I.; Ko, J.; Pak, K.; Choi, S. Q.; Kim, I.-D.; Park, S., Large-Area Synthesis of Ultrathin, Flexible, and Transparent Conductive Metal–Organic Framework Thin Films via a Microfluidic-Based Solution Shearing Process. *Adv. Mater.* **2022,** *34* (12), 2107696.
42. Chen, C.; Shan, Z.; Tao, S.; Xie, A.; Yang, H.; Su, J.; Horke, S.; Kitagawa, S.; Zhang, G., Atomic Tuning in Electrically Conducting Bimetallic Organic Frameworks for Controllable Electromagnetic Wave Absorption. *Adv. Funct. Mater.* **2023,** *33* (45), 2305082.
43. Yang, C.; Dong, R.; Wang, M.; Petkov, P. S.; Zhang, Z.; Wang, M.; Han, P.; Ballabio, M.; Bräuninger, S. A.; Liao, Z.; Zhang, J.; Schwotzer, F.; Zschech, E.; Klauss, H.-H.; Cánovas, E.; Kaskel, S.; Bonn, M.; Zhou, S.; Heine, T.; Feng, X., A semiconducting layered metal-organic framework magnet. *Nat. Commun.* **2019,** *10* (1), 3260.
44. Damacet, P.; Hannouche, K.; Gouda, A.; Hmadeh, M., Controlled Growth of Highly Defected Zirconium–Metal–Organic Frameworks via a Reaction–Diffusion System for Water Remediation. *ACS Appl. Mater. Interfaces.* **2024**. doi.org/10.1021/acsami.3c16327
45. Park, J. H.; Paczesny, J.; Kim, N.; Grzybowski, B. A., Shaping Microcrystals of Metal–Organic Frameworks by Reaction–Diffusion. *Angew. Chem. Int. Ed.* **2020,** *59* (26), 10301-10305.
46. Esquirol, A.-L.; Sarazin, P.; Virgilio, N., Tunable Porous Hydrogels from Cocontinuous Polymer Blends. *Macromolecules* **2014,** *47* (9), 3068-3075.
47. Shimizu, Y.; Matsui, J.; Unoura, K.; Nabika, H., Liesegang Mechanism with a Gradual Phase Transition. *J. Phys. Chem. B.* **2017,** *121* (11), 2495-2501.
48. Ackroyd, A. J.; Holló, G.; Mundoor, H.; Zhang, H.; Gang, O.; Smalyukh, I. I.; Lagzi, I.; Kumacheva, E., Self-organization of nanoparticles and molecules in periodic Liesegang-type structures. *Sci. Adv.* **2021,** *7* (16), eabe3801.
49. Morse, H. W.; Pierce, G. W., Diffusion and Supersaturation in Gelatine. *Proc. Am. Acad. Arts Sci.* **1903,** *38* (22), 625-648.
50. Xing, Z.; Zhang, G.; Ye, J.; Zhou, Z.; Gao, J.; Du, B.; Yue, K.; Wang, Q.; Liu, J., Liesegang Phenomenon of Liquid Metals on Au Film. *Adv. Mater.* **2023,** *35* (7), 2209392.
51. George, J.; Varghese, G., Liesegang patterns: Estimation of diffusion coefficient and a plausible justification for colloid explanation. *Colloid. Polym. Sci.* **2002,** *280*, 1131-1136.
52. Bertasa, M.; Dodero, A.; Alloisio, M.; Vicini, S.; Riedo, C.; Sansonetti, A.; Scalarone, D.; Castellano, M., Agar gel strength: A correlation study between chemical composition and rheological properties. *Eur. Polym. J.* **2020,** *123*, 109442.
53. Walimbe, P.; Itatani, M.; Kulkarni, P.; Lagzi, I.; Kulkarni, S., A Quasi Universal Matalon–Packter Law for a Periodically Precipitating System of Iron(II) Hydroxide Involving Volumes and Concentrations of the Invading Electrolyte. *Langmuir* **2023,** *39* (38), 13420-13429.
54. Ban, T.; Nagatsu, Y.; Tokuyama, H., Propagation Properties of the Precipitation Band in an AlCl3/NaOH System. *Langmuir* **2016,** *32* (2), 604-610.
55. Büki, A.; Kárpáti-Smidróczki, É.; Zrínyi, M., Computer simulation of regular Liesegang structures. *J. Chem. Phys.* **1995,** *103* (23), 10387-10392.
56. Itatani, M.; Fang, Q.; Nabika, H., Modification of the Matalon–Packter Law for Self-Organized Periodic Precipitation Patterns by Incorporating Time-Dependent Diffusion Flux. *J. Phys. Chem. B.* **2021,** *125* (25), 6921-6929.
57. Sheberla, D.; Sun, L.; Blood-Forsythe, M. A.; Er, S.; Wade, C. R.; Brozek, C. K.; Aspuru-Guzik, A.; Dincă, M., High Electrical Conductivity in Ni3(2,3,6,7,10,11-hexaiminotriphenylene)2, a Semiconducting Metal–Organic Graphene Analogue. *J. Am. Chem. Soc.* **2014,** *136* (25), 8859-8862.
58. Li, H.; Evans, A. M.; Castano, I.; Strauss, M. J.; Dichtel, W. R.; Bredas, J.-L., Nucleation–Elongation Dynamics of Two-Dimensional Covalent Organic Frameworks. *J. Am. Chem. Soc.* **2020,** *142* (3), 1367-1374.
59. Castano, I.; Evans, A. M.; Li, H.; Vitaku, E.; Strauss, M. J.; Brédas, J.-L.; Gianneschi, N. C.; Dichtel, W. R., Chemical Control over Nucleation and Anisotropic Growth of Two-Dimensional Covalent Organic Frameworks. *ACS Cent. Sci.* **2019,** *5* (11), 1892-1899.
60. Evans, A. M.; Parent, L. R.; Flanders, N. C.; Bisbey, R. P.; Vitaku, E.; Kirschner, M. S.; Schaller, R. D.; Chen, L. X.; Gianneschi, N. C.; Dichtel, W. R., Seeded growth of single-crystal two-dimensional covalent organic frameworks. *Science* **2018,** *361* (6397), 52-57.
61. Li, H.; Evans, A. M.; Dichtel, W. R.; Bredas, J.-L., Quantitative Description of the Lateral Growth of Two-Dimensional Covalent Organic Frameworks Reveals Self-Templation Effects. *ACS mater. lett* **2021,** *3* (4), 398-405.
62. Castano, I.; Evans, A. M.; Reis, R. d.; Dravid, V. P.; Gianneschi, N. C.; Dichtel, W. R., Mapping Grains, Boundaries, and Defects in 2D Covalent Organic Framework Thin Films. *Chem. Mater.* **2021,** *33* (4), 1341-1352.
63. Itatani, M.; Fang, Q.; Unoura, K.; Nabika, H., Role of Nuclei in Liesegang Pattern Formation: Insights from Experiment and Reaction-Diffusion Simulation. *J. Phys. Chem. C.* **2018,** *122* (6), 3669-3676.
64. Antal, T.; Droz, M.; Magnin, J.; Pekalski, A.; Rácz, Z., Formation of Liesegang patterns: Simulations using a kinetic Ising model. *J. Chem. Phys.* **2001,** *114* (8), 3770-3775.
65. Cotton, F.; Francis, R., Sulfoxides as ligands. I. A preliminary survey of methyl sulfoxide complexes. *J. Am. Chem. Soc.* **1960,** *82* (12), 2986-2991.
66. Meek, D. W.; Straub, D. K.; Drago, R. S., Transition metal ion complexes of dimethyl sulfoxide. *J. Am. Chem. Soc.* **1960,** *82* (23), 6013-6016.
67. Song, Q.; Shi, S.; Liu, B., Metal-Organic Framework-Based Colloidal Particle Synthesis, Assembly, and Application. *ChemPlusChem* **2023,** *88* (2), e202200396.
68. Wang, J.; Imaz, I.; Maspoch, D., Metal–Organic Frameworks: Why Make Them Small? *Small. Struct.* **2022,** *3* (1), 2100126.
69. Yan, W.; Guo, Z.; Xu, H.; Lou, Y.; Chen, J.; Li, Q., Downsizing metal–organic frameworks with distinct morphologies as cathode materials for high-capacity Li–O 2 batteries. *Mater. Chem. Front* **2017,** *1* (7), 1324-1330.
70. Habeeb, O. A.; Kanthasamy, R.; Ali, G. A.; Sethupathi, S.; Yunus, R. B. M., Hydrogen sulfide emission sources, regulations, and removal techniques: a review. *Rev. Chem. Eng.* **2018,** *34* (6), 837-854.
71. Verma, G.; Gokarna, A.; Kadiri, H.; Nomenyo, K.; Lerondel, G.; Gupta, A., Multiplexed Gas Sensor: Fabrication

Strategies, Recent Progress, and Challenges. *ACS Sens.* **2023,** *8* (9), 3320-3337.
72. Xie, L. S.; Skorupskii, G.; Dincă, M., Electrically Conductive Metal–Organic Frameworks. *Chem. Rev.* **2020,** *120* (16), 8536-8580.
73. Choi, J.-M.; Byun, J.-H.; Kim, S. S., Influence of grain size on gas-sensing properties of chemiresistive p-type NiO nanofibers. *Sensor Actuat B: Chem* **2016,** *227*, 149-156.
74. Li, Y.; Li, L.; Zhang, R.; Ying, Z.; Zhou, Y.; Wu, W.; Wang, G., Effect of SnO2 particle size on gas-sensing performance for ppb-level NO2 at room temperature under UV light. *J. Mater. Sci. Mater. Electron.* **2024,** *35* (3), 236.
75. Stolz, R. M.; Kolln, A. F.; Rocha, B. C.; Brinks, A.; Eagleton, A. M.; Mendecki, L.; Vashisth, H.; Mirica, K. A., Epitaxial Self-Assembly of Interfaces of 2D Metal–Organic Frameworks for Electroanalytical Detection of Neurotransmitters. *ACS Nano* **2022,** *16* (9), 13869-13883.
76. Panayotov, D. A.; Burrows, S. P.; Morris, J. R., Infrared Spectroscopic Studies of Conduction Band and Trapped Electrons in UV-Photoexcited, H-Atom n-Doped, and Thermally Reduced TiO2. *J. Phys. Chem. C.* **2012,** *116* (7), 4535-4544.
77. Zhang, Y.; Han, Y.; Deng, F.; Zhao, T.; Liu, Z.; Wang, D.; Luo, J.; Yu, Y., Enhancement of the performance of Ge–air batteries under high temperatures using conductive MOF-modified Ge anodes. *Carbon Energy* **2024**, e580.
78. Zhao, X.; Jiang, S.; Zhang, Z.; Yan, X.; Xu, Z.; Hu, H.; Zhu, Y.; Attfield, J. P.; Yang, M., High-Performance H2S Sensors to Detect SF6 Leakage. *ACS Sens.* **2024,** *9* (10), 5512-5519.
79. Wu, X.; Tian, X.; Zhang, W.; Peng, X.; Zhou, S.; Buenconsejo, P. J. S.; Li, Y.; Xiao, S.; Tao, J.; Zhang, M., Solution-Processable MOF-on-MOF System Constructed via Template-Assisted Growth for Ultratrace H2S Detection. *Angew. Chem.* **2024**, e202410411.
80. Ali, F. I. M.; Awwad, F.; Greish, Y. E.; Mahmoud, S. T., Hydrogen Sulfide (H2S) Gas Sensor: A Review. *IEEE Sens. J.* **2019,** *19* (7), 2394-2407.
81. Matsuoka, R.; Sakamoto, R.; Kambe, T.; Takada, K.; Kusamoto, T.; Nishihara, H., Ordered alignment of a one-dimensional π-conjugated nickel bis(dithiolene) complex polymer produced via interfacial reactions. *Chem. Commun.* **2014,** *50* (60), 8137-8139.
82. Fu, Q.; Liu, H.; Tang, X.; Wang, R.; Chen, M.; Liu, Y., Multifunctional Two-Dimensional Polymers for Perovskite Solar Cells with Efficiency Exceeding 24%. *ACS Energy Lett* **2022,** *7* (3), 1128-1136.
83. Chen, L.; Gong, C.; Wang, X.; Dai, F.; Huang, M.; Wu, X.; Lu, C.-Z.; Peng, Y., Substoichiometric 3D Covalent Organic Frameworks Based on Hexagonal Linkers. *J. Am. Chem. Soc.* **2021,** *143* (27), 10243-10249.
84. Kwon, O. S.; Hong, J.-Y.; Park, S. J.; Jang, Y.; Jang, J., Resistive Gas Sensors Based on Precisely Size-Controlled Polypyrrole Nanoparticles: Effects of Particle Size and Deposition Method. *J. Phys. Chem. C.* **2010,** *114* (44), 18874-18879.

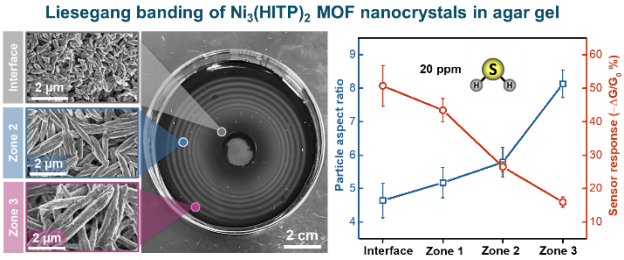

TOC